Nano Research

Open Access

Research Article

Laser direct writing of flexible multifunctional airflow sensors on the Kevlar fabric

Wei Wang[1,3] ✉, Zi-Qing Chen[2], Yong-Qi Li[2], Yu-Long Wang[2], Mei-Chen Liu[1], Yun-Bo Ruan[3], Yang Zhang[4], Shu-Juan Liu[2] ✉, and Qiang Zhao[1,2] ✉

[1] College of Electronic and Optical Engineering and College of Flexible Electronics (Future Technology), Nanjing University of Posts and Telecommunications, Nanjing 210023, China
[2] State Key Laboratory of Organic Electronics and Information Displays and Jiangsu Key Laboratory for Biosensors, Institute of Advanced Materials (IAM), Nanjing University of Posts and Telecommunications, Nanjing 210023, China
[3] Zhe Jiang Topsun Logistic Control CO., LTD., Yuhuan 317600, China
[4] Department of Rehabilitation Medicine, School of Acupuncture-Moxibustion and Tuina and School of Health Preservation and Rehabilitation, Nanjing University of Chinese Medicine, Nanjing 210023, China

Cite this article: *Nano Research*, **2025**, *18*, 94907062. https://doi.org/10.26599/NR.2025.94907062

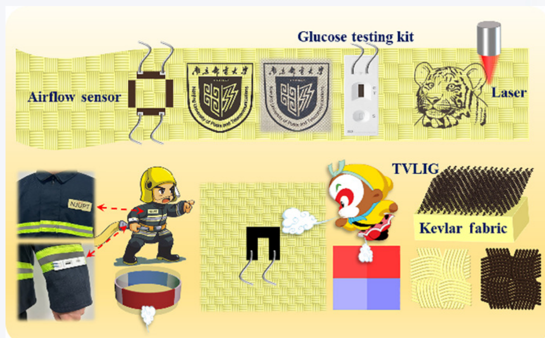

ABSTRACT: The growing interest in flexible devices has emerged as a global trend due to their advantages in flexibility, lightweight structure, and wearability, addressing the limitations of traditional devices. While wearable airflow sensors have been previously reported, the development of flexible fabric-based airflow sensors capable of functioning in environments with open flames—critical for fire rescue operations—has yet to be explored, largely due to the poor fire resistance of conventional fabrics. In this work, we first present a flexible, wearable, and multifunctional airflow sensor with excellent fire-resistant properties, fabricated through a simple direct laser writing process. This sensor maintains airflow detection capabilities even in the presence of open flames. Typically, the fabrication of fabric-based sensors involves complex procedures such as carbon materials doping or vapor-phase deposition, leading to lengthy preparation cycles and high costs. Furthermore, fabric-based devices are inherently prone to flammability. To address these challenges, we introduce twice-vertical laser-induced graphene (TVLIG) as a sensitive and reliable component for fire-resistant airflow sensors. The resulting TVLIG/Kevlar fabric can be integrated into various garments, particularly protective suits, to form sensitive and fire-resistant airflow sensors capable of detecting airflow velocity and direction in both two-dimensional (2D) and three-dimensional (3D) spaces during fire incidents. Additionally, the TVLIG patterns can be expanded to multifunctional platforms, such as glucose detection for injured individuals, offering further applications in rescue operations. This functional expansion reduces the burden on rescue personnel and streamlines device preparation. With its outstanding sensing capabilities, fire resistance, and expandability, the developed flexible airflow sensor shows great potential for various real-world rescue scenarios, promising advancements in wearable sensing technology for rescue engineering.

KEYWORDS: flexible airflow sensor, direct laser writing, twice-vertical laser-induced graphene, fire accident rescue, Kevlar fabric

1 Introduction

In recent years, the rapid development of flexible electronic devices has gained significant attention [1], with numerous applications emerging in areas such as health monitoring devices [2–4], medical implants [5–7], wearable electronics [8–10], soft actuators [11–13], and flexible sensors [14–16]. As essential components of modern electronics, sensors play a critical role in the integration of these systems. Among various types, airflow sensors are often overlooked, despite their importance in detecting airflow direction and velocity for industries such as coal mining [17], aerospace [18], weather forecasting [19], environmental monitoring [20], and emergency rescue [21].

Received: August 5, 2024; **Revised:** September 25, 2024
Accepted: October 2, 2024

✉Address correspondence to Qiang Zhao, iamqzhao@njupt.edu.cn; Wei Wang, wangwei29@njupt.edu.cn; Shu-Juan Liu, iamsjliu@njupt.edu.cn

Airflow sensors provide accurate detection of environmental airflow direction and velocity, allowing for real-time responses to sudden changes. The importance of this functionality has led to significant research in the field. However, most conventional airflow sensors are developed on rigid substrates, lacking the flexibility required for modern applications. For example, Takahashi et al. proposed a pitot tube-based airflow sensor with a microelectromechanical system (MEMS) structure on a rigid substrate, offering compact size and high resolution for airflow velocity measurements [22]. Similarly, spherical airflow vector sensors with rigid substrates have demonstrated excellent performance for in-flight wind detection in unmanned aerial vehicle (UAV) [23]. Despite their effectiveness, these rigid sensors often suffer from complex preparation processes and high production costs, limiting their integration with flexible electronic systems. This shortcoming hinders their potential application in scenarios such as real-time airflow monitoring in rescue operations. To address these limitations, research on flexible airflow sensors has recently gained momentum. For example, flexible graphene airflow sensors with microdot arrays exhibits fast response times, low detection limits, and broad detection ranges [24]. Additionally, Zhang et al. developed an ultrasensitive and textile-based flexible airflow sensor using carbonized silk fabric and carbon nanotubes, achieving a response time of 1.3 s and the ability to detect airflow velocities as low as 0.05 ms^{-1} [25].

Flexible device substrates can be categorized into two types: flexible polymers, such as polyimide [19], and fabrics [26]. While polymer substrates offer customizability and material diversity, they often suffer from poor breathability when worn on the human body. Conversely, fabric-based devices provide superior breathability, making them more comfortable for wearable applications [21, 27]. As the proverb goes: "Every coin has its two sides", fabric substrates also come with two major disadvantages: poor fire resistance and complex fabrication processes, which often involve carbon materials doping or vapor-phase deposition, leading to long preparation cycles and high cost. These challenges limit the development of simple and efficient methods for producing flexible and fire-resistant sensors for applications such as protective gear in rescue engineering.

Direct laser writing (DLW) has emerged as a powerful, precise [28–30], and programmable technique for microfabrication, offering maskless patterning and position-selective capabilities [31–33]. Our previous work demonstrated the potential of DLW in creating smart Marangoni actuators on various substrates, including polyimide and polydimethylsiloxane [34, 35]. DLW enables simplified fabrication processes and reduced costs through fine patterning without the need for masks [36, 37]. Graphene, known for its exceptional electrical and mechanical properties, has become a cornerstone in sensor development [38, 39]. High-quality graphene can be efficiently prepared via DLW method, also referred to as laser-induced graphene (LIG) [40]. However, to date, DLW and LIG have not been utilized for the development of flexible fabric-based fire-resistant airflow sensors, largely due to challenges in integrating graphene patterns with fabrics that meet perfect sensing, strength and fire-retardant performance requirements.

In this work, we present the first report on the development of a flexible, wearable, and multifunctional airflow sensor with excellent fire-resistant properties using DLW. Kevlar, an aramid textile renowned for its mechanical toughness and fire resistance, was also called "armored defender", and was selected as the substrate for DLW. The airflow-sensitive LIG array was efficiently and precisely patterned onto the Kevlar fabric. The resulting flexible airflow sensors is capable of detecting airflow direction and velocity in both two-dimensional (2D) and three-dimensional (3D) spaces. Importantly, the inherent fire resistance and mechanical toughness of the Kevlar fabric enable the sensor to withstand sharp object damage and fire exposure, surpassing most previously reported fabric sensors in fire resistance. These wearable airflow sensors have demonstrated their suitability for disaster relief scenarios, such as fire rescue, by providing real-time monitoring of airflow impact on fire dynamics. Moreover, with the multifunctional capabilities of LIG, the Kevlar-based sensor platform can be adapted for other applications, such as glucose detection in rescue scenarios, demonstrating the versatility and scalability of Kevlar-based airflow sensors throughout the rescue process. The combination of mechanical toughness, fire resistance, and scalable functionality, along with the simplicity of DLW fabrication, paves the way for the development of integrated disaster relief equipment. This work highlights the significant potential of flexible fabric-based airflow sensors for cutting-edge applications in flexible electronics and rescue engineering.

2 Results and discussion

The construction of the conductivity is critical for flexible fabric sensors, as it requires the precise patterning of conductive materials on specific regions of the fabric. Recently, DLW has been demonstrated as a powerful technology for precise, programmable, and position-selective microfabrication, making it ideal for the selective preparation of conductive materials. In this work, commercial Kevlar fabric was chosen as the flexible substrate due to its exceptional toughness and fire resistance, as well as its chemical composition, which supports transformation under laser treatment. The aromatic repeat units in Kevlar play a crucial role in graphene formation under laser processing. The mechanism behind LIG formation is attributed to the laser-triggered rearrangement of aromatic compounds into the graphitic structures. LIG, with its excellent conductivity, serves as an ideal material for smart sensors, and its microstructure significantly influences electrical resistance, reflecting the relationship between external forces and electrical properties. As shown in Fig. 1(a), a key advantage of laser fabrication is the ability to create high-precision patterns without the need for masks. As a proof of concept, a school logo and a delicate tiger head were fabricated, demonstrating the high precision of DLW. The diagrammatic sketches of airflow sensors and glucose detectors further illustrate this concept. The high precision of DLW is evident, as even the fine details of the tiger's eyes and whiskers are clearly identified (Fig. 1(b)). During DLW, the original Kevlar fabric is divided into two layers: an upper carbonized layer, induced by the laser, and a lower unprocessed layer that retains its Kevlar properties and acts as a support (Fig. 1(c)). The laser not only facilitates carbon materials formation but also constructs microstructures. These microstructural changes impact the material's electrical properties by altering conductive pathways, enhancing sensitivity to environment changes, and enabling airflow sensor functionality by responding to external forces, such as those generated by airflow (Fig. 1(d)). Kevlar, originally light yellow and featuring a cross-weave pattern, is composed of benzene ring repeating units linked to amide groups. Strong covalent bonds exist between the aromatic nuclei and the imides, while additional hydrogen bonds connect the carbonyl and

清华大学出版社 Tsinghua University Press | SciOpen

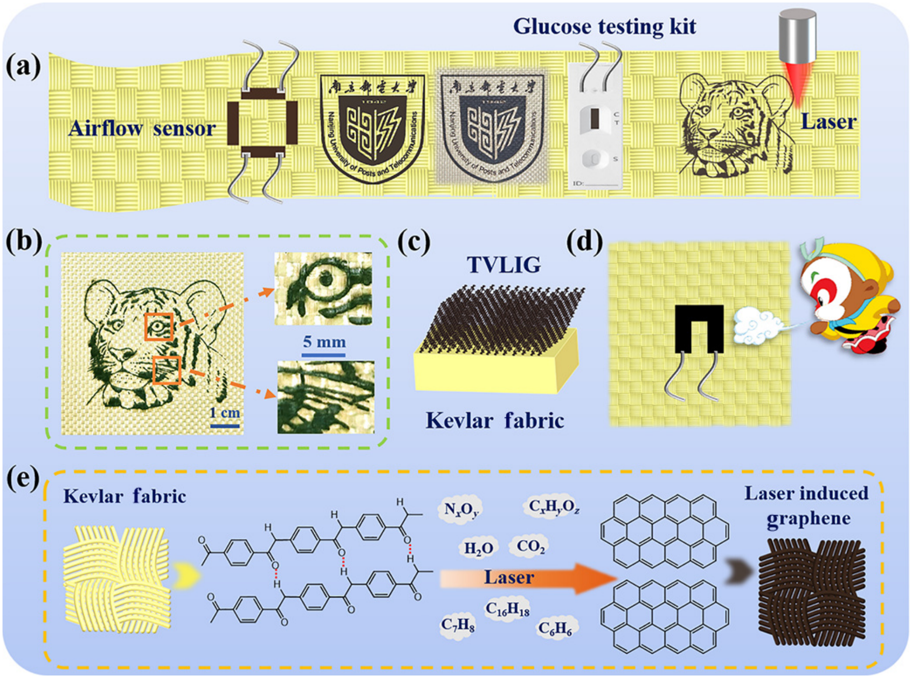

Figure 1 (a) Schematic illustration of the fabrication processes of TVLIG fabric for developing flexible multifunctional airflow sensors. (b) The photograph of laser patterned LIG tiger head. (c) Schematic diagram of the cross-section of TVLIG/Kevlar fabric after laser treatment. (d) The airflow sensor based on TVLIG. (e) Schematic illustration of the transformation of Kevlar to LIG.

N–H groups. Laser processing enables high-precision interactions between the laser and material, inducing novel transformations through photochemical and photophysical reactions. In this work, the localized high temperatures generated by the laser cause depolymerization of the Kevlar fibers, breaking C–O and N–C bonds (Fig. 1(e)). The resulting atoms reassemble to form molecules such as CO_2, H_2O, and N_xO_y, along with benzene derivatives like C_6H_6, C_7H_8, $C_{16}H_{18}$, and pyrolytic compounds $(C_xH_yO_z)_2$. Crucially, the remaining carbon atoms recrystallize into brownish-black carbon materials with excellent conductivity.

To examine the effect of laser power on the carbonization of Kevlar, we performed Raman spectra on LIG samples produced at various laser power settings, while keeping the writing speed and laser scribing spacing constant (Fig. 2(a)). The original Kevlar fabric exhibited multiple characteristic peaks in its Raman spectrum, but three dominant peaks—corresponding to the D, G, and 2D peaks of graphene—became apparent in the laser-processed areas. The three peaks, occurring at ~ 1350, ~ 1502, and ~ 2700 cm^{-1}, respectively, confirm the successful formation of LIG on the Kevlar fabric. To further investigate the effects of laser parameters on LIG quality and sensor performance, we compared single-process LIG (SLIG) with twice-vertical LIG (TVLIG). Firstly, the applied laser power can be divided into ways including the single processing and twice-vertical processing. Secondly, making the total laser power of two processing equal to the single processing, for example, a laser power of 6.4 W for SLIG, 5.6–0.8 W, and 3.2–3.2 W for TVLIG. As shown in Fig. 2(a), the 2D peak forSLIG was relatively subdued, indicating a lower degree of graphitization. However, increasing the number of the laser passes and optimizing the power distribution significantly improved LIG quality. The D, G, and 2D peaks in TVLIG were more pronounced, and the peak value increased with the second laser power applied. The ratio of D to G peaks intensities (I_D/I_G) decreased from 0.48 to 0.15 when comparing TVLIG processed at 5.6–0.8 W versus 3.2–3.2 W. These results demonstrate that average laser power yields better graphitization with fewer defects.

X-ray photoelectron spectroscopy (XPS) of TVLIG (5.6–0.8 W) further confirmed the improved graphitization (Fig. 2(b)). Carbon content increased from 77.52% (original Kevlar) to 90.26% (TVLIG), while oxygen content decreased from 16.45% to 7.04%. Nitrogen content showed a slight decrease from 6.04% to 2.7%.

Furthermore, as shown in Fig. 2(c), the C 1s spectrum of Kevlar were deconvoluted into three peaks centered at 284.5 (C–C), 286 (C–N), and 289.1 (C=O). While the C 1s spectrum of TVLIG were deconvoluted into four peaks centered at 284.5 (C–C), 285.6 (C–N), 289.1 (C=O), and 287.2 (C–O) (Fig. 2(d)). Notably, the number of carbon atoms bonded to nitrogen decreased sharply, while carbon–carbon bonding increased. However, the total content of oxygen atoms still decreased as well as the carbon atoms increased. These XPS results, combined with the Raman spectra, indicate localized graphitization in the laser-treated areas, with sp^2-carbon networks dominating in TVLIG. As discussed above, some gas molecules like CO_2 will be produced and escaped from the surface of Kevlar during DLW, leading to the formation of porous surface of TVLIG. The scanning electron microscopy (SEM) images proved that the TVLIG has the porous structures from interior to surface at the microscopic level (Figs. 3(c) and 3(d)), in contrast to the smooth and ordered fiber arrangement of the original Kevlar fabric (Figs. 3(a) and 3(b)). While laser processing effectively altered the surface morphology of Kevlar, the overall fabric structure remained intact, preserving its mechanical properties. The above results proved that DLW method can effectively modify the microstructure and properties of Kevlar, which in turn influences the conductivity of TVLIG/Kevlar. To further optimize the sensing properties of the TVLIG/Kevlar fabric, a series of experiments were conducted to systematically investigate the relationship between the laser process and microstructure. Conventional laser preparation methods typically use unidirectional single-pass processing,

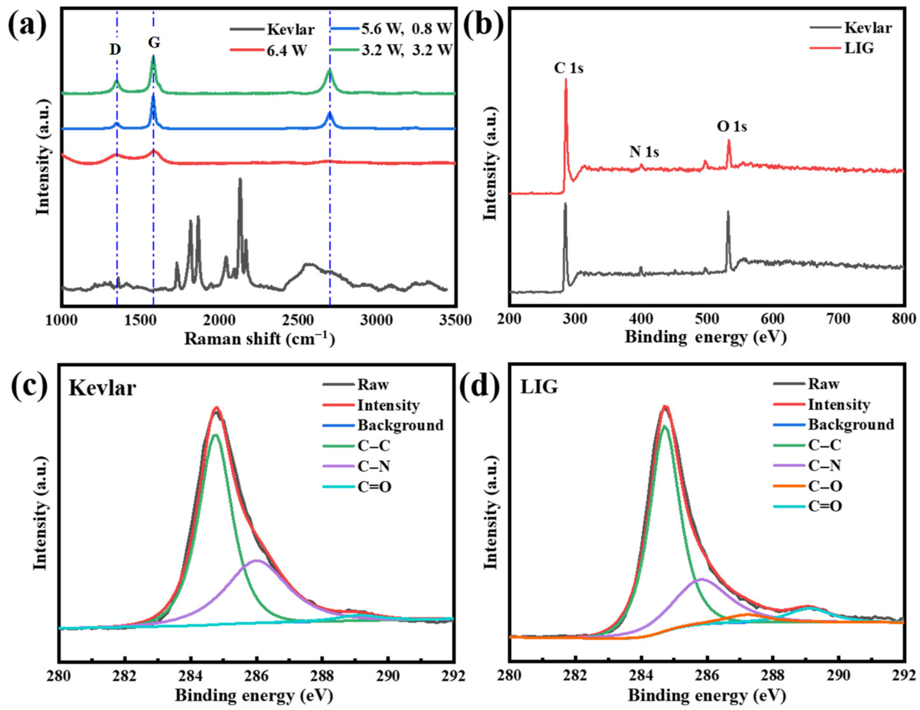

Figure 2 (a) Raman spectra of the LIG prepared with different laser powers. (b) XPS spectra of the Kevlar and TVLIG. High-resolution XPS C 1s spectra of (c) a Kevlar fabric and (d) the TVLIG, respectively.

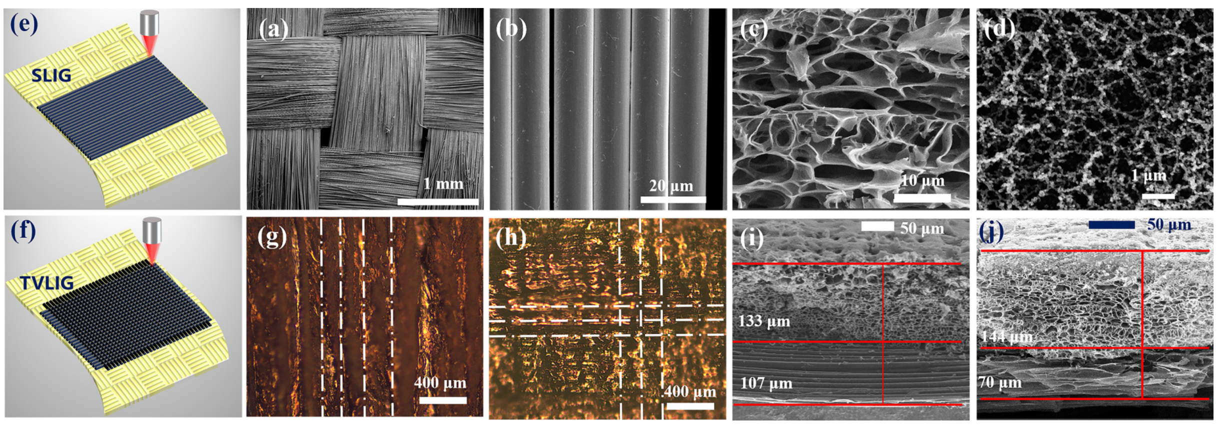

Figure 3 (a) and (b) Field-emission SEM images of the surface morphology of Kevlar fabric. (c) and (d) High-resolution SEM images of TVLIG. Schematic diagrams of surface structures of (e) SLIG and (f) TVLIG. The optical microscope photographs of (g) SLIG and (h) TVLIG. The section views of (i) SLIG and (j) TVLIG.

generating patterned parallel grooves, as shown in Fig. 3(e), which refers to it as SLIG. However, for airflow sensors, the ability to detect small disturbances is crucial. Compared to parallel grooves, cross-shaped groove structures produce more independent units, leading to more pronounced and responsive changes in structure and electrical properties. Consequently, as shown in Fig. 3(f), the cross microstructure, prepared by two intersecting laser paths, exhibits a lower sensing threshold and a wider range of resistance variation than the parallel microstructure. SEM images and optical microscope photographs clearly depict the grooves on the LIG surface after laser processing, and the parallel microstructure corresponding to unidirectional single laser direct writing and the cross microstructure corresponding to two crossed laser direct writing have been proved clearly (Figs. 3(g) and 3(h)). The design of cross-shaped grooves creates more independent microstructural units, which respond more actively to external stimuli. The cross-section images of SEM of laser-treated Kevlar reveal the junction between LIG and Kevlar, showing that appropriate laser parameters maintain the LIG on the Kevlar substrate, which is beneficial for future applications in wearable flexible electronics. The cross-section image of SLIG (Fig. 3(i)) shows a thickness of ~ 110 μm, while the retained Kevlar measures ~ 92 μm. Additionally, the cross section of SLIG displays high porosity. The second laser processing step increases the thickness of TVLIG to ~ 119 μm, with the stacking of graphene layers consistent with the Raman spectroscopy results (Fig. 3(j)). The Kevlar thickness decreases slightly but remains stable when using a laser power of 5.6–0.8 W, suggesting that TVLIG may offer better sensing performance than SLIG.

The laser parameters not only affect the microstructure of LIG but also influence its conductivity, which is critical for the performance of flexible electronic devices. Therefore, constructing and optimizing the conductivity of flexible fabric sensors warrants close attention. Three key parameters can be adjusted during laser fabrication procedure, including line spacing, laser power, and laser

清華大学出版社 Tsinghua University Press | SciOpen

velocity. As shown in Fig. 4(a), the resistance (R) of SLIG increases significantly with increasing line spacing, with resistance variations spanning three orders of magnitude. This is likely due to the reduced laser-treated area and decreased connectivity between LIG regions as line spacing increases. For example, when line spacing exceeds 2 mm, the laser-treated Kevlar remains an insulator, while reducing the spacing to 0.5 mm lowers resistance to ~ 4.6 Ω. Conversely, increasing laser power reduces resistance, as shown in Fig. 4(b), with the lowest resistance (3.14 Ω) observed at 16 W. However, exceeding this power level damages the Kevlar substrate. Resistance changes more gradually between 8 and 16 W. Similarly, increasing laser speed decreases the laser energy imparted to the Kevlar, resulting in a positive correlation between resistance and scanning speed (Fig. 4(c)). Below 100 mm/s, scanning speed has minimal effect on resistance, but at higher speeds, resistance increases due to reduced heat accumulation from the faster laser movement of laser spot. In conclusion, lower scanning speed, higher laser power, and smaller line spacings generally improve LIG conductivity, but excessive adjustments to these factors may damage the Kevlar substrate. A balance must be struck between optimal laser parameters and device integrity. The same considerations apply to TVLIG, which was found to have slightly lower resistance than SLIG during volt–ampere testing (Fig. 4(d)). Importantly, the cross-shaped structure of TVLIG enhances sensitivity without increasing resistance. For airflow sensors, the key issue is how changes in electric resistance reflect sensing ability. Since laser parameters affect the resistance of TVLIG, they also influence its sensing performance. The porous frame structure of TVLIG can deform under external force, improving inter-layer interactions and altering the overall resistance, thereby reflecting airflow conditions. The porosity of TVLIG provides multiple branches for electron transport, enhancing conductivity, but it also provides the potential to further reduce resistance. The application of external force, such as airflow, may compress the TVLIG branches, reducing pores and decreasing resistance. To evaluate sensor performance, the change in resistance before and after airflow exposure on TVLIG (ΔR) was expressed in absolute terms. Tests on the switching ratio of resistance ($\Delta R/R$) under an air velocity of 3.2 ms^{-1} were conducted to assess the effects of various laser parameters. The airflow sensors were designed in a U-shape, with a pattern measuring 1.5 cm × 1.5 cm, and copper tape with conductive silver paste was applied to ensure stable electrical contact at both ends. Firstly, the effects of laser power and scanning speed on single-process SLIG were evaluated, as shown in Figs. 5(a) and 5(b). As laser power increased, the switching ratio of SLIG resistance initially rose and then fell, exhibiting a similar trend with changes in scanning speed. SLIG achieved the highest current variation at a laser power of 6 W, with stability and a high switching ratio observed at 6.4 W. Secondly, the TVLIG, which involves two laser processing steps, was studied. In addition, the curve with the maximum switching ratio also shows well response-recovery time. The data showed that its response time is 284 ms and recovery time is 335 ms (Fig. S1 in the Electronic Supplementary Material (ESM)), which are basically consistent with the current existing reports. As shown in Fig. 5(c), the resistance switching ratios for TVLIG at 3.2–3.2 W and 5.6–0.8 W were relatively large and comparable. The total laser power of the two processes was kept constant. As described earlier, smaller line spacings improve conductivity, so the line spacings for the two laser processes were set at 0.05 and 0.1 mm. The results proved that the 0.05 mm/0.1 mm group had a higher switching ratio than the of 0.05 mm/0.05 mm group, as excessively small line spacing may damage previous LIG layers, compromising conductivity. Finally, the switching ratios of SLIG (0.15) and TVLIG (0.2) confirmed that the cross-shaped microstructure of TVLIG produces a more positive and pronounced response to external force when using the same laser scanning speed and line spacing (Fig. 5(e)). Based on the above findings, the optimal laser parameters for airflow sensor fabrication

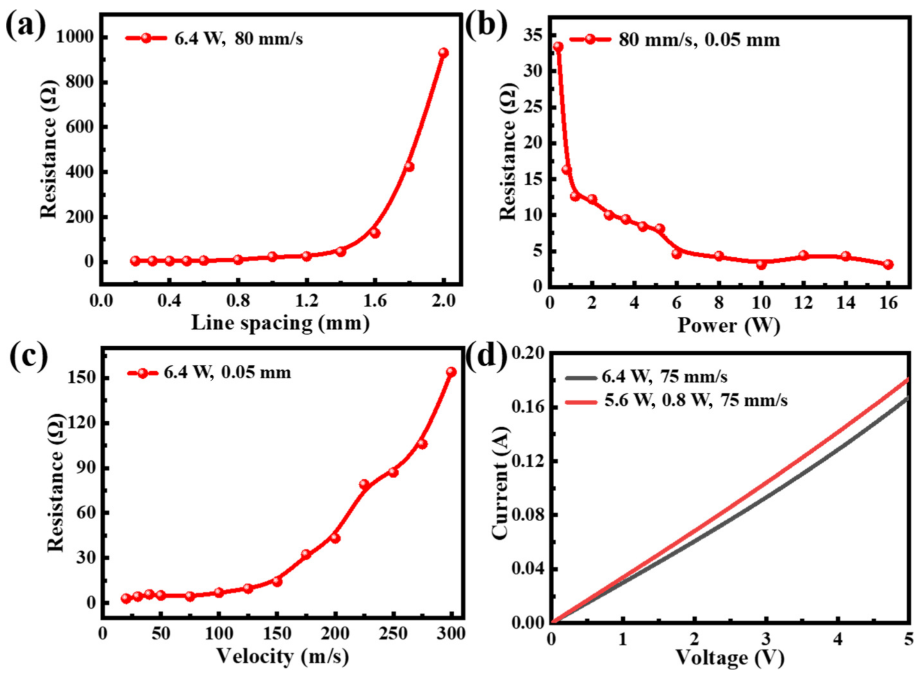

Figure 4 (a) Resistance of SLIG samples produced by different line spacings under a fixed scan rate and laser power. (b) Resistance of SLIG samples produced by different scan rates under a fixed laser power and line spacing. (c) Resistance of SLIG samples produced by different laser powers under a fixed scan rate and line spacing. (d) The comparison of resistance of SLIG and TVLIG under different voltages.

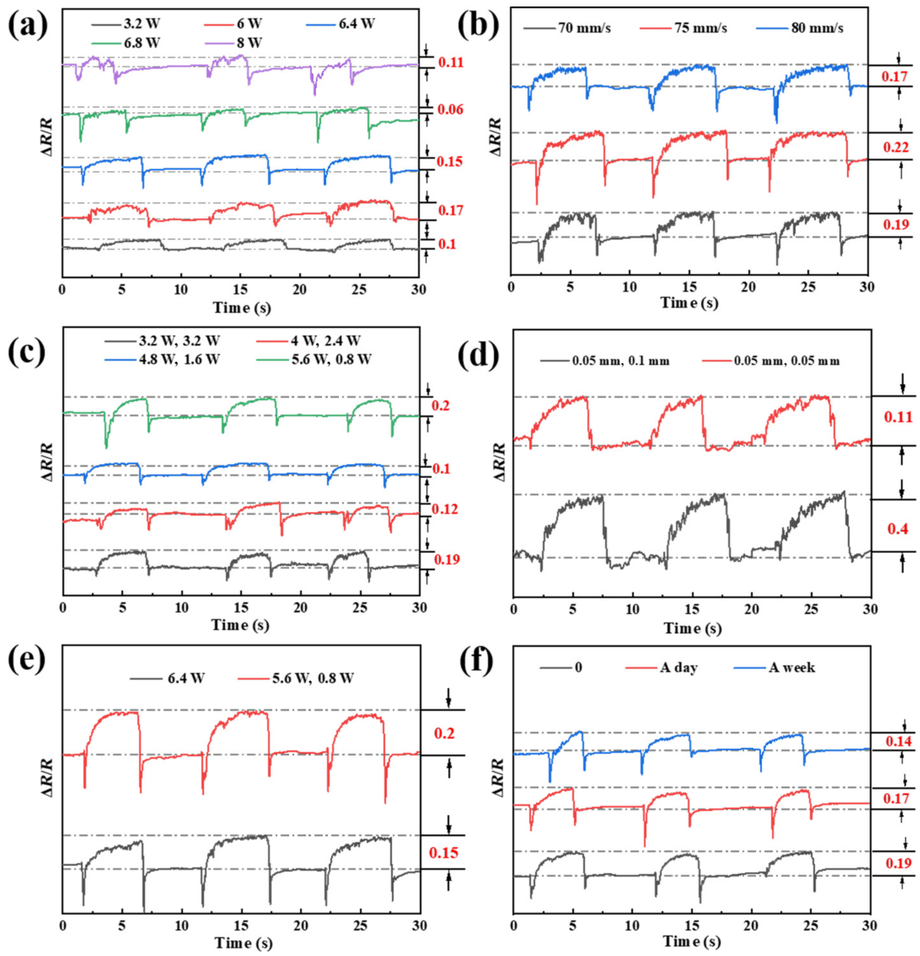

Figure 5 (a) Switching characteristics of SLIG with different laser powers. (b) Switching characteristics of SLIG with different scanning speeds. (c) Switching characteristics of TVLIG with different laser powers. (d) Switching characteristics of TVLIG with different line spacings. (e) The comparison of switching characteristics of SLIG and TVLIG. (f) Stability of switching characteristics at different time.

were determined to be a power of 5.6–0.8 W, a line spacing of 0.05 mm/0.1 mm, and a scanning speed of 75 mm/s. Additionally, the stability of the sensor was confirmed, with only slight fluctuations in the switching ratio observed after one week of testing, indicating reliable and consistent performance (Fig. 5(f)).

To further explore the application of airflow sensors based on TVLIG, we conducted experiments to accurately identify different airflow velocities. Performance tests of the flexible fabric airflow sensor at various airflow rates were performed to assess the response performance of the TVLIG sensor to different airflow conditions. As shown in Fig. 6(a), the switching ratio of sensor increased significantly as the airflow speed rose from 0 m/s to approximately 4 m/s, with each airflow speed within the effective range being identified accurately. However, the switching ratio plateaued once airflow speeds exceeded 4 m/s, which is consistent with the performance of most reported flexible airflow sensors [19, 25, 41]. A common limitation of fabric-based sensors is their susceptibility to damage from strong external forces, yet the TVLIG/Kevlar airflow sensor not only withstands airflow speeds up to 8 m/s, but also provides real-time feedback, confirming its ability to detect the airflow under extreme weather conditions. Moreover, the TVLIG sensor demonstrated reliable signal transmission even after being cut with scissors. Long-term and multi-cycle testing further confirmed its durability.

Figure 6(b) compares the switching curve of the TVLIG airflow sensor after 500 consecutive cycles with its first cycle, revealing only a alight slight deviation in waveform. The sensor successfully captured airflow changes with excellent repeatability. When we accumulated the switch ratios of multiple cycles in chronological order, we found that the airflow sensor can catch up every change accurately, as well as perfect repeatability, and there is no significant deviation between peak and valley values basically within 500 s (Fig. 6(c)). The same sensor can also achieve stable recognition of the number of cycles and airflow velocity in multiple cyclic tests with continuous changes in different wind speeds (Fig. 6(d)). Whether for different airflow velocities or multiple cycles, its recognition performance is stable and reliable. Based on the characteristics of the sensor, we further calibrated its hysteresis and repeatability (Figs. 6(e) and 6(f)) according to the equations of hysteresis and repeatability

$$\delta_{\mathrm{H}} = \pm(\Delta H_{\max}/Y_{\mathrm{FS1}}) \times 100\% \quad (1)$$

$$\delta_{\mathrm{R}} = \pm(\Delta R_{\max}/Y_{\mathrm{FS2}}) \times 100\% \quad (2)$$

In the hysteresis test, the sensor is continuously measured in the wind field, where the wind speed increases continuously from 0 to 4 m/s and then gradually decreases from 4 to 0 m/s. The $\Delta H_{\max}$ refers to the maximum difference between the up and down rows, and Y_{FS1} refers to the maximum range. The repeatability test here

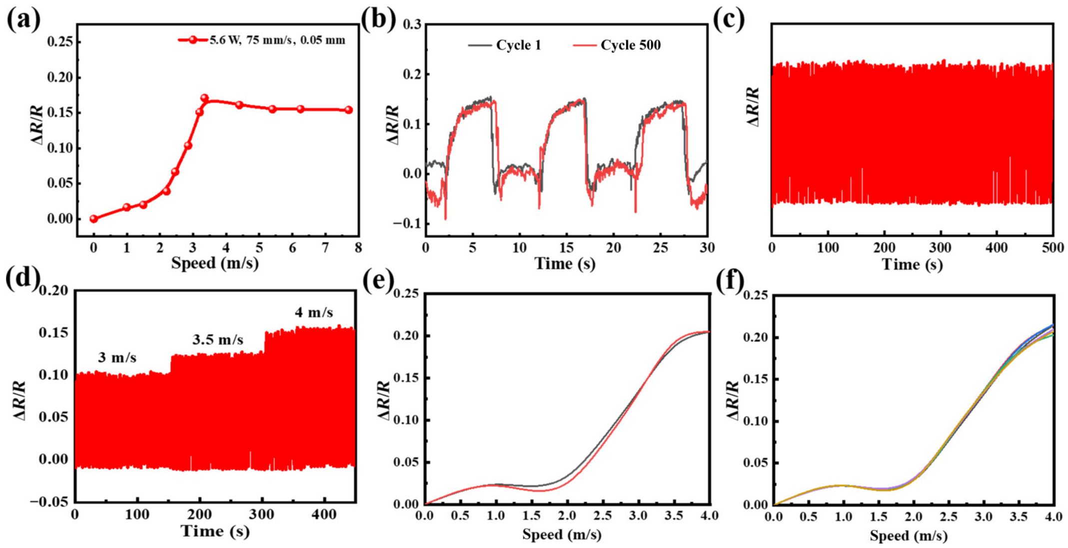

Figure 6 (a) Relative current variation within the airflow range of 0.00–8.00 m/s. (b) Stability of switching characteristics. (c) Cycling performance of TVLIG at the airflow speed of 3.2 m/s. (d) Cycling performance of TVLIG at various airflow speeds including 3, 3.5, and 4 m/s. (e) The test of hysteresis of airflow sensors. (f) The test of repeatability of airflow sensors.

refers to testing the same sensor outputs in wind speed from 0 to 4 m/s three times. And test the sensor outputs three more times for wind speeds ranging from 4 to 0 m/s again. ΔR_{max} refers to the maximum difference between the upstream or the downstream. Y_{FS2} refers to the maximum range. Therefore, the data showed that ΔH_{max} is 0.00819, Y_{FS1} is 0.205, ΔR_{max} is 0.007, and Y_{FS2} is 0.2102. Therefore, according to Eqs. (1) and (2), δ_H is 3.995%, and δ_R is 3.333%. The results of hysteresis and repeatability strongly demonstrate the well consistency of sensor outputs when exposed to repeated identical flow conditions. The above results lay the groundwork for practical applications of TVLIG-based airflow sensors in flexible and wearable sensor made from Kevlar fabric.

Airflow sensors find utility across various industries, such as coal mining, aerospace, weather forecasting, environmental monitoring, and emergency rescue. In recent years, rescue operations in extreme scenarios have gained increasing attention due to their life-saving potential, making advanced sensors indispensable for modern rescue technologies. The TVLIG/Kevlar-based airflow sensor holds significant promise for fire accident rescue due to its unique capabilities. Kevlar, known as the “armor defender”, is widely used in military applications for its toughness, fire resistance, and flexibility, and is now also being applied to emergency rescue.

To assess the toughness of the TVLIG/Kevlar airflow sensor in fire accident applications, tests were conducted using ordinary scissors to cut the sensor, the sensor’s resistance fluctuated slightly during cutting (Fig. S2 in the ESM), but the fabric sensor remained was not undamaged. Once the scissors were removed, the resistance stabilized, demonstrating the sensor’s resilience (Movie ESM1). The superior toughness of the TVLIG/Kevlar sensor suggests its greater potential in rescue scenarios compared to ordinary fabric-based sensors. Beyond Kevlar’s intrinsic properties, the capabilities of TVLIG should be emphasized. Accurately identifying airflow direction is crucial for rescue personnel in fire situations, as sudden changes in airflow can drastically influence fire behavior, posing a serious threat to lives and property. To demonstrate this, four rectangular TVLIG airflow sensors were arranged tangentially around a cylinder, in a head to tail manner and formed a 90° tangent with the cylinder, enabling them to receive airflow from 360°. As shown in Fig. 7(a), the sensors, labeled 1 through 4, detected airflow independently based on switching ratios when airflow hit their respective surfaces. Each airflow direction generated a specific combination of switching ratios, enabling accurate wind direction identification (Fig. 7(b)). For instance, when airflow was directed perpendicular to sensor 3, it experienced the greatest force, resulting in the highest switching ratio (~ 0.2), while sensor 1, on the opposite side, registered the lowest value (~ 0). The angle between the sensors 2 and 4 and the airflow direction is almost 0°, meaning the smaller force received compared to sensor 3. The switching ratio of them is around 0.1 because of the formation of included angle with airflow. A similar principle can also be extended to other airflow directions. The combination of switching ratios of four sensors can reflect the airflow direction exactly when the airflow is perpendicular to the sensor surface or called in 3D plane. While most existing airflow sensors rely on being perpendicular to airflow for detection, because this method can apply the force generated by the airflow to the sensor effectively, and the sensor maximizes its detection effect. However, this orientation is difficult to maintain in real-world conditions. To address this, we tested the TVLIG/Kevlar sensors arranged in a 2D plane, forming a square and positioned parallel to airflow. This setup allowed the sensors to detect airflow from the side (Fig. 7(c)), taking advantage of the synergistic effect of macro-porosity of the Kevlar fabric and the micro-porosity of TVLIG. When airflow hit the corners of the square, any adjacent sensors exhibited similar switching ratios. For example, if the airflow blows from the junction of the sensors 2 and 3, the switching ratio of them will be similar, as well as the switching ratio of the sensors 1 and 4, and the former being greater than the latter due to closer to the airflow and the greater force it experiences, as shown in Fig. 7(d). When airflow was directed along the square’s edges, three distinct switching ratios were observed, with the sensor closest to the airflow showing the highest value, and the sensor furthest from the airflow showing the lowest (Fig. 7(e)). There are also a pair of sensors in the middle distance between them, and their switching ratio values also belong to moderate level. This combination of switching ratios from the four sensors enabled precise airflow direction identification in both

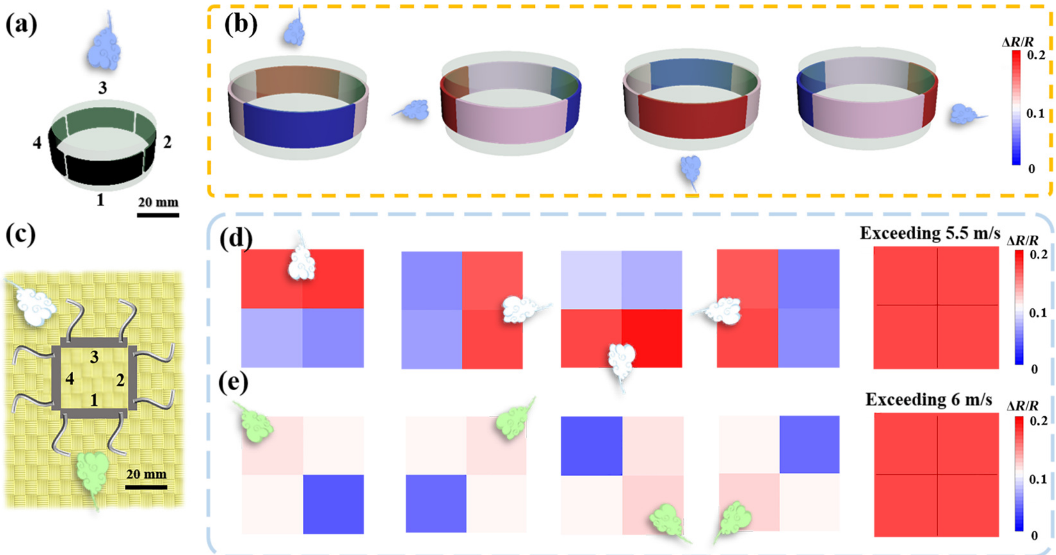

Figure 7 (a) Schematic of a cylinder with a rectangular TVLIG sensor. (b) Sensing of wind sources at different locations in 3D plane. (c) Schematic of a flat surface with a rectangular TVLIG sensor. (d) Sensing of wind sources at different locations when the direction of airflow faces the corners of a square. (e) Sensing of wind sources at different locations when the direction of airflow faces the edges of a square.

2D and 3D spaces. These findings confirm the sensor's feasibility for detecting airflow direction and velocity in rescue scenarios. However, each sensor has maximum threshold that can withstand airflow velocity.

As shown in the last two images of Figs. 7(d) and 7(e), when all sensors in the module group exceed the threshold, the sensor group will not be able to accurately identify the source of airflow, which means that this identification method has usage limitations. The airflow hit the sensor group from the long side of the rectangular and the speed exceeds 5.5 m/s, the four sensors cannot show significant differences, and their switching ratio values all reach around 0.2. While the threshold is up to 6 m/s when airflow hits it from the rectangular group corner, because the airflow path is longer than former and reduces the airflow intensity. Therefore, the recognition threshold of the sensor group varies according to the airflow direction and velocity.

Leveraging the advantages of Kevlar fabric, TVLIG-based sensors can be integrated into ordinary or special protective clothing, such as fire-protection suits (Figs. 8(a) and 8(b)). Using DLW, a TVLIG pattern of the NJUPT logo was inscribed on Kelvar. This pattern serves as both a functional airflow sensor and a decorative element in a fire-protection suit. Wires connected to the sensor ends allow signal transmission to a bluetooth module inside the protective clothing. Given the dynamic movement of clothing during rescue operations, the sensor's flexibility was tested by bending it into a circle (Movie ESM2). No significant changes or damage to the sensor's appearance were observed, and continuous voltammetry measurements showed no fluctuations in resistance, confirming the sensor's flexibility (Fig. S3 in the ESM). In addition to bending performance, the tensile performance of fabrics also affects the clothing comfort and the practical application of sensors. We further tested the impact of DLW on Kevlar tensile performance. As shown in Fig. S4(a) in the ESM, the maximum tensile strength of original Kevlar is ~ 200 N, while the maximum tensile strength of TVLIG/Kevlar is around 170 N, because the structure of original Kevlar has been changed by DLW. Even though their fibers occurred rupture under maximum tension, TVLIG still exhibits good conductivity. TVLIG/Kevlar can still play a certain role under high tension. The conductivity properties of TVLIG/Kevlar in cyclic tensile forces of different sizes were studied, such as 6.8, 12, 33, 40, 50, and 60 N, and they all showed good repeatability and stability (Figs. S4(b)–S4(g) in the ESM). As the pulling force increases, the initial resistance increases (Fig. S4(h) in the ESM), because the pulling force caused TVLIG structure to change from compact to gap connected, leading to the resistance increased. Therefore, the morphology change caused by DLW will not significantly affect the bending and stretching ability of the original Kevlar. In fire accidents, high temperature and flammability are the main threats to electronic devices, particularly fabric-based ones. These limitations restrict the application and development of fabric electronics in rescue operations. However, the TVLIG/Kevlar airflow sensor, with its excellent fire resistance, shows great potential for these extreme environments. High temperature is main threat for fabric-based sensor, and the relationships among temperature, resistance, and airflow intensity are crucial. Many previous works have proved that the resistance of LIG increases with the rise of temperature [42–44], and our experiment results also keep the consistency with above conclusion. The LIG conductivity is mainly determined by its carrier concentration and mobility. At low temperatures, the carrier mobility of graphene is relatively high, while the phonons (lattice vibrations) in graphene are enhanced at high temperatures, leading to phonons to significantly increase the scattering of electrons, which reduces the carrier mobility. The increase in phonon scattering usually has a more significant impact on the resistance, therefore, the resistance of LIG usually increases with increasing temperature. As shown in Fig. 8, the initial resistance value of TVLIG would impact the resistance variation and final switching ratio. As the temperature rises, the switching ratio of sensor decreased slightly under the same airflow condition. For example, when the sensor faced the same wind speed of 4 m/s, the switching ratio can reach 0.15 at 50 °C, decrease to 0.13 at 70 °C, and continue to decrease at 90 °C (Fig. 8(e)). When the temperature continues to rise to a threshold value (~ 120 °C), regardless of whether the temperature continues to rise, the switch ratio shows a same phenomenon (Fig. 8(f)). That is why the switching ratio of sensor is only related to the wind speed and

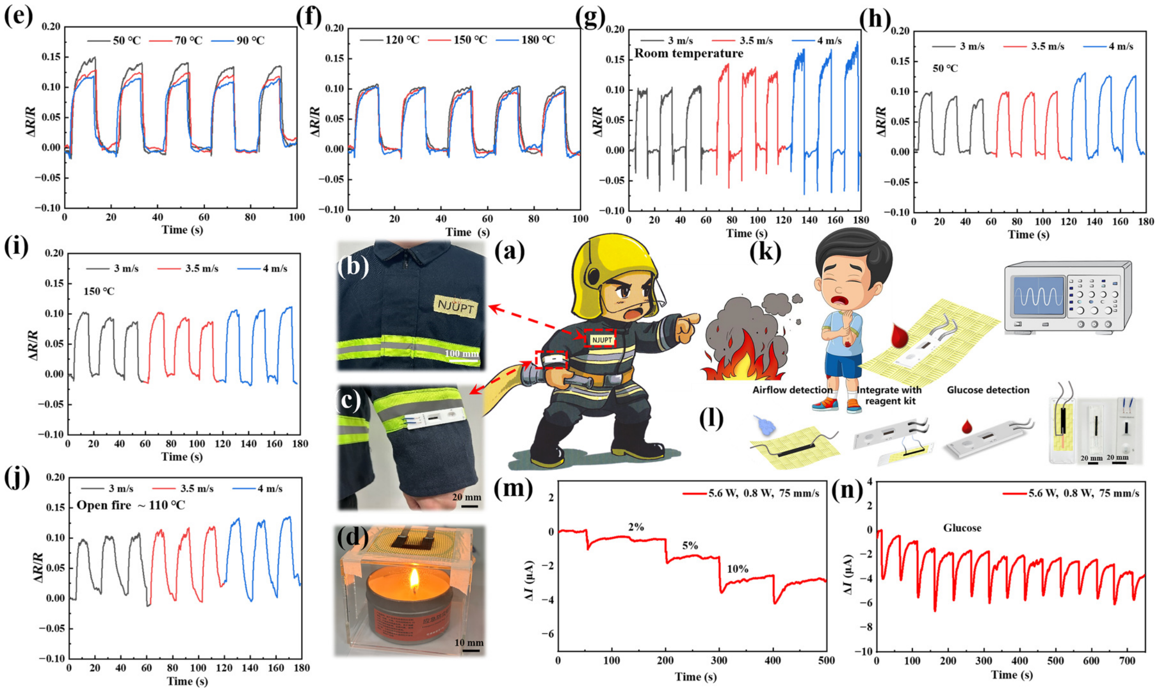

Figure 8 (a) and (b) TVLIG as an airflow sensor integrated into a fire suit. (c) Physical image of the TVLIG/Kevlar kit sewn onto clothing. (d) Physical diagram of airflow sensor testing sensing performance under a lit candle. (e) and (f) The switching ratios of sensor under different temperature conditions. (g)–(i) The relationship between different temperatures and various airflow velocities of sensors. (j) The sensing performance of fabric-based sensor at the present of open fire. (k) and (l) The schematic diagrams for the modification and integration of the airflow sensor to the glucose detection kit. (m) Current changes at different glucose concentrations of TVLIG's kit. (n) Cyclic testing of the reagent kit at the same glucose concentration.

not to the temperature when exceeding the temperature threshold. We further investigated the sensing ability of sensors to airflow intensity at different temperatures in detail. As shown in Fig. 8(g), at room temperature, the sensor exhibits the most significant switching ratio for different airflow intensities, and the higher the airflow velocity, the greater the switching ratio. The switching ratio gradually decreases at 50 and 150 °C. But the cyclic curve is still obvious (Figs. 8(h) and 8(i)), indicating that even though the sensor cannot effectively distinguish the airflow velocity at high temperatures, it has not been damaged and can effectively distinguish the appearance and direction of airflow. To further evaluate its performance in a simulated fire scenario, a lit candle was placed beneath the sensor (Fig. 8(d)). Despite exposure to an open flame, the sensor provided reliable responses to varying airflow velocities, and the temperature of sensor is approximately 110 °C under the stable outputs (Fig. 8(j)). In conclusion, the identification ability of sensors to airflow intensity decreased with temperature increasing and it cannot identify different airflow intensities when the temperature exceeded 120 °C. But that does not mean that the device is damaged or there is a lack of airflow direction monitoring. The sensor remained functional, demonstrating repeatable responses even in the presence of fire. In brief, we have demonstrated that the TVLIG/Kevlar airflow sensor holds great promise for fire rescue applications, offering multidimensional support by detecting airflow velocity, 2D, and 3D directions, and providing flexibility and fire resistance. Notably, following a disaster, casualties often exhibit abnormal physiological indicators, necessitating medical equipment for monitoring. However, additional medical equipment increases the burden on rescuers and it may bring new obstacle. Fortunately, the functionality of the TVLIG/Kevlar sensor can be extended to a multifunction rescue platform. By integrating TVLIG/Kevlar into an empty commercial reagent kit pre-sewn into clothing (Fig. 8(c)), the sensor can detect glucose concentrations, providing clear electronic signal. The detailed process of modification and integration is shown in the Figs. 8(k) and 8(l), the airflow sensor is removed from original location, a portion of the pre-sewn reagent kit is opened, it is aligned with Kevlar/TVLIG, and the original internal wires are threaded through the two openings at the bottom of the kit to transmit signals. During the integration process, the test strips that transmit liquid flow inside the reagent kit are retained and combined with TVLIG for better delivery of blood towards TVLIG direction. Further observation devices on the backend can timely read the waveform of the sensor to determine the glucose level. Tests confirmed the sensor's ability to detect glucose concentration of 2%, 5%, and 10% (Fig. 8(m)). We further tested multiple cycles of sensing glucose solution. As shown in Fig. 8(n), the sensor kit can accurately identify multiple testing cycles. However, the overall baseline shows a slow downward trend, because the increased accumulation of glucose on TVLIG leads to changes in resistance. Continuous measurements can still be taken to ensure its practical application. The detection capability originates from the graphene's large surface area, excellent conductivity, and high electrocatalytic performance, which enhance sensitivity. The integration of glucose detection functionality into rescue operations reduces the burden on rescue personnel and lower sensor cost. Furthermore, we also look forward to more reports of research and applications about the detection of TVLIG/Kevlar for other substances.

3 Conclusions

In conclusion, we have demonstrated the preparation of patterned TVLIG on flexible Kevlar fabric as a conductive module for fire-resistant airflow sensors. The TVLIG can be freely patterned on Kevlar using twice-vertical DLW technology, and has shown greater sensitivity compared to conventional LIG in airflow sensing. The porosity and flexibility of TVLIG contribute to the creation of wearable airflow sensor with enhanced responsiveness. Optimal laser parameter combinations were identified, yielding high-quality graphene and improved sensing performance. The TVLIG/Kevlar-based airflow sensor accurately detects airflow velocity and distinguishes airflow direction in both 2D and 3D spaces, forming matrix arrays to represent airflow direction and magnitude. Furthermore, the fire-resistant properties of the sensor allow it to be integrated into protective suits, making it suitable for fire rescue applications. The robustness, flexibility, and fire resistance of TVLIG/Kevlar demonstrate its strong potential for use in extreme environments. Additionally, the TVLIG/Kevlar platform can be extended for multifunctional applications, such as glucose detection in medical rescue scenarios. This expansion of functionality not only eases the burden on rescue personnel but also reduces sensor production costs. We believe that the TVLIG serves as sensitive, fire-resistant, and stable airflow sensor module, facilitating the development of flexible and wearable fabric sensors based on Kevlar, with significant promise for rescue engineering and other cutting-edge applications.

4 Methods

4.1 Fabrication of laser-induced graphene/Kevlar textile

A piece of commercial Kevlar fabric was used as the raw material. The fabric was thoroughly cleaned in an ultrasonic cleaner with acetone, alcohol, and deionized (DI) water in sequence. After drying, a computer-controlled commercial CO_2 laser cutting system was used to pattern the surface of the Kevlar fabric with pre-designed shapes. All laser processing was performed in ambient air. After laser treatment, the Kevlar fabric remained flexible, retaining its ability to bend and adhere to other flexible materials.

4.2 Characterization

The SEM images were obtained by a JEOL field-emission scanning electron microscope (JSM-7500). The ESCALAB 250 spectrometer provided the corresponding XPS spectra. Raman spectra were obtained through a JOBIN YVON T64000 instrument equipped with an excitation source of liquid-nitrogen-cooled argon-ion laser at 532 nm (Spectra-Physics Stabilite 2017). Moreover, the applied laser power was approximately 30 μW, and the average spot diameter was 1 μm, measured with a long-working distance objective (50×).

4.3 Resistance testing of sensors

A commercial CO_2 laser was used to print 10 mm × 10 mm squares on the surface of the Kevlar fabric, and the resistance was measured using a four-probe square resistance tester, with each sample tested five times (n = 5). Resistance values were presented as the mean ± standard deviation.

4.4 Flow sensing tests

Copper tape was applied to the poles of the fabricated sensor, followed by fixation with silver paste. Wires were connected to an electrochemical workstation for electrical measurements, which were carried out at room temperature. The sensor was tested under a bias voltage of 1 V. The air velocity was measured with a velocimeter (AS-8336), and airflow was maintained at a constant rate of 3.2 ms^{-1}. Sensitivity and stability were evaluated by calculating $(R - R_0)/R_0$, where R and R_0 represent the sensor's resistance during airflow was on and off, respectively.

For wind direction detection in the vertical direction, four printed 40 mm × 8 mm rectangular sensor devices were uniformly attached to the surface of a circular device. Airflow was switched on and off at fixed intervals, and the electrical signals from all four sensors were recorded simultaneously. Four positions were measured.

For wind direction detection in the side direction, a pattern of 40 mm × 8 mm rectangles was designed and printed. The fabricated sensor devices were fixed to the surface of a carton using paper tape. Airflow was switched on and off at regular intervals, and electrical signals from all four sensors were measured concurrently. Eight positions were measured.

4.5 Glucose concentration test

The laser-machined devices were secured to a table surface and connected to the electrochemical workstation using copper tape and wires. Glucose solution was applied near the device, and the electrical response of the device to different glucose concentrations was measured using the electrochemical workstation.

Electronic Supplementary Material: Supplementary material (further details of response-recovery time of sensors, toughness, bending and tensile performance of sensors, and related videos) is available in the online version of this article at https://doi.org/10.26599/NR.2025.94907062.

Data availability

All data needed to support the conclusions in the paper are presented in the manuscript and the Electronic Supplementary Material. Additional data related to this paper may be requested from the corresponding author upon request.

Acknowledgements

This work was supported by the National Natural Science Foundation of China (Nos. 62205157 and 82302847), China Postdoctoral Science Foundation (No. 2023M731777), the Natural Science Research Start-up Foundation of Recruiting Talents of Nanjing University of Posts and Telecommunications (No. NY222010), and Funding Matching Project for the National Natural Science Foundation of China of Nanjing University of Chinese Medicine (No. XPT82302847).

Declaration of competing interest

All the contributing authors report no conflict of interests in this work.

Author contribution statement

W. W.: Data curation, project administration, validation, writing manuscript, experimental design, funding acquisition. Z.-Q. C., Y.-Q. L., Y.-L. W., M.-C. L., and Y.-B. R.: Data curation, project administration, validation, experimental design. Y. Z.: Project administration, funding acquisition. S.-J. L. and Q. Z.: Project administration, revised manuscript. All the authors have approved the final manuscript.

Use of AI statement

None.

References

[1] Zhang, D. D.; Ren, Y. X.; Barbot, A.; Seichepine, F.; Lo, B.; Ma, Z. C.; Yang, G. Z. Fabrication and optical manipulation of micro-robots for biomedical applications. *Matter* **2022**, *5*, 3135–3160.

[2] Yu, H.; Yang, X. N.; Lian, Y. L.; Wang, M. Y.; Liu, Y. M.; Li, Z.; Jiang, Y. D.; Gou, J. An integrated flexible multifunctional wearable electronic device for personal health monitoring and thermal management. *Sens. Actuators A: Phys.* **2021**, *318*, 112514.

[3] Wang, Z. Y.; Bu, M. M.; Xiu, K. H.; Sun, J. Y.; Hu, N.; Zhao, L. B.; Gao, L. X.; Kong, F. Z.; Zhu, H.; Song, J. et al. A flexible, stretchable and triboelectric smart sensor based on graphene oxide and polyacrylamide hydrogel for high precision gait recognition in Parkinsonian and hemiplegic patients. *Nano Energy* **2022**, *104*, 107978.

[4] Hu, Y. G.; Zhao, T.; Zhu, P. L.; Zhang, Y.; Liang, X. W.; Sun, R.; Wong, C. P. A low-cost, printable, and stretchable strain sensor based on highly conductive elastic composites with tunable sensitivity for human motion monitoring. *Nano Res.* **2018**, *11*, 1938–1955.

[5] Ma, Z. C.; Zhang, Y. L.; Han, B.; Hu, X. Y.; Li, C. H.; Chen, Q. D.; Sun, H. B. Femtosecond laser programmed artificial musculoskeletal systems. *Nat. Commun.* **2020**, *11*, 4536.

[6] Wang, Z. Y.; Ma, Z. T.; Sun, J. Y.; Yan, Y. H.; Bu, M. M.; Huo, Y. M.; Li, Y. F.; Hu, N. Recent advances in natural functional biopolymers and their applications of electronic skins and flexible strain sensors. *Polymers* **2021**, *13*, 813.

[7] Yi, L. Y.; Hou, B.; Liu, X. G. Optical integration in wearable, implantable and swallowable healthcare devices. *ACS Nano* **2023**, *17*, 19491–19501.

[8] Li, S. B.; Li, M.; Chen, L.; Xu, X. H.; Cui, A. Y.; Zhou, X.; Jiang, K.; Shang, L. Y.; Li, Y. W.; Zhang, J. Z. et al. Ultra-stable, endurable, and flexible $Sb_2Te_xSe_{3-x}$ phase change devices for memory application and wearable electronics. *ACS Appl. Mater. Interfaces* **2022**, *14*, 45600–45610.

[9] Sun, J. Y.; Xiu, K. H.; Wang, Z. Y.; Hu, N.; Zhao, L. B.; Zhu, H.; Kong, F. Z.; Xiao, J. L.; Cheng, L. J.; Bi, X. Y. Multifunctional wearable humidity and pressure sensors based on biocompatible graphene/bacterial cellulose bioaerogel for wireless monitoring and early warning of sleep apnea syndrome. *Nano Energy* **2023**, *108*, 108215.

[10] Mathai, A. R. P.; Stalin, T.; Alvarado, P. V. Y. Flexible fiber inductive coils for soft robots and wearable devices. *IEEE Rob. Autom. Lett.* **2022**, *7*, 5711–5718.

[11] Wang, W.; Zhang, Y. L.; Han, B.; Ma, J. N.; Wang, J. N.; Han, D. D.; Ma, Z. C.; Sun, H. B. A complementary strategy for producing moisture and alkane dual-responsive actuators based on graphene oxide and PDMS bimorph. *Sens. Actuators B: Chem.* **2019**, *290*, 133–139.

[12] Wang, W.; Zhang, Y.; Zhang, Y. L.; Zhang, J. R.; Sun, X. C.; Han, D. D.; Sun, H. B. Multicoating nanoarchitectonics for facile preparation of multi-responsive paper actuators. *ACS Appl. Mater. Interfaces* **2022**, *14*, 27242–27250.

[13] Xin, C.; Ren, Z. G.; Zhang, L. R.; Yang, L.; Wang, D. W.; Hu, Y. L.; Li, J. W.; Chu, J. R.; Zhang, L.; Wu, D. Light-triggered multi-joint microactuator fabricated by two-in-one femtosecond laser writing. *Nat. Commun.* **2023**, *14*, 4273.

[14] Nakajima, T.; Fujio, Y.; Sugahara, T.; Tsuchiya, T. Flexible ceramic film sensors for free-form devices. *Sensors* **2022**, *22*, 1996.

[15] Huo, Y. M.; Bu, M. M.; Ma, Z. T.; Sun, J. Y.; Yan, Y. H.; Xiu, K.; Wang, Z. Y.; Hu, N.; Li, Y. F. Flexible, non-contact and multifunctional humidity sensors based on two-dimensional phytic acid doped co-metal organic frameworks nanosheets. *J. Colloid Interface Sci.* **2022**, *607*, 2010–2018.

[16] Yin, F. F.; Guo, Y. J.; Li, H.; Yue, W. J.; Zhang, C. W.; Chen, D.; Geng, W.; Li, Y.; Gao, S.; Shen, G. Z. A waterproof and breathable cotton/rGO/CNT composite for constructing a layer-by-layer structured multifunctional flexible sensor. *Nano Res.* **2022**, *15*, 9341–9351.

[17] Zhou, L.; Thomas, R. A.; Yuan, L.; Bahrami, D. Experimental study of improving a mine ventilation network model using continuously monitored airflow. *Min., Metall. Explor.* **2022**, *39*, 887–895.

[18] Sung, W. T.; Chen, K. Y.; Hsu, Y. C. Design a breeze sensor system based on electric field via two-elemental direction. *Expert Syst. Appl.* **2011**, *38*, 5584–5590.

[19] Huang, L. B.; Liu, Y.; Li, G.; Song, Y.; Su, J. J.; Cheng, L.; Guo, W. H.; Zhao, G. G.; Shen, H. C.; Yan, Z. et al. Ultrasensitive, fast-responsive, directional airflow sensing by bioinspired suspended graphene fibers. *Nano Lett.* **2023**, *23*, 597–605.

[20] Fei, F.; Zhou, S. L.; Mai, J. D.; Li, W. J. Development of an indoor airflow energy harvesting system for building environment monitoring. *Energies* **2014**, *7*, 2985–3003.

[21] Luo, Y.; Miao, Y. P.; Wang, H. M.; Dong, K.; Hou, L.; Xu, Y. Y.; Chen, W. C.; Zhang, Y.; Zhang, Y. Y.; Fan, W. Laser-induced Janus graphene/poly(p-phenylene benzobisoxazole) fabrics with intrinsic flame retardancy as flexible sensors and breathable electrodes for fire-fighting field. *Nano Res.* **2023**, *16*, 7600–7608.

[22] Takahashi, H.; Nakai, A.; Shimoyama, I. Waterproof airflow sensor for seabird bio-logging using a highly sensitive differential pressure sensor and nano-hole array. *Sens. Actuators A: Phys.* **2018**, *281*, 243–249.

[23] Haneda, K.; Matsudaira, K.; Noda, R.; Nakata, T.; Suzuki, S.; Liu, H.; Takahashi, H. Compact sphere-shaped airflow vector sensor based on mems differential pressure sensors. *Sensors* **2022**, *22*, 1087.

[24] Song, Y. H.; Chen, L.; Yang, Q. Q.; Liu, G.; Yu, Q. W.; Xie, X. Y.; Chen, C.; Liu, J.; Chao, G. Q.; Chen, X. et al. Graphene-based flexible sensors for respiratory and airflow monitoring. *ACS Appl. Nano Mater.* **2023**, *6*, 8937–8944.

[25] Jiang, Q. Y.; Li, R.; Wang, F.; Shi, X. F.; Chen, F. X.; Huang, Y.; Wang, B. S.; Zhang, W. S.; Wu, X. K.; Wei, F.; et al. Ultrasensitive airflow sensors based on suspended carbon nanotube networks. *Adv. Mater.* **2022**, *34*, 2107062.

[26] Rao, Y. F.; Yuan, M.; Gao, B.; Li, H.; Yu, J. B.; Chen, X. P. Laser-scribed phosphorus-doped graphene derived from Kevlar textile for enhanced wearable micro-supercapacitor. *J. Colloid Interface Sci.* **2023**, *630*, 586–594.

[27] Wang, H. M.; Wang, H. M.; Wang, Y. L.; Su, X. Y.; Wang, C. Y.; Zhang, M. C.; Jian, M. Q.; Xia, K. L.; Liang, X. P.; Lu, H. J. et al. Laser writing of janus graphene/Kevlar textile for intelligent protective clothing. *ACS Nano* **2020**, *14*, 3219–3226.

[28] Xu, K. C.; Cai, Z. M.; Luo, H. Y.; Lin, X. Y.; Yang, G.; Xie, H. B.; Ko, S. H.; Yang, H. Y. An *in-situ* hybrid laser-induced integrated sensor system with antioxidative copper. *Int. J. Extreme Manuf.* **2024**, *6*, 065501.

[29] Yu, H. Y.; Gai, M. X.; Liu, L.; Chen, F. R.; Bian, J.; Huang, Y. Laser-induced direct graphene patterning: From formation mechanism to flexible applications. *Soft Sci.* **2023**, *3*, 4.

[30] Xu, K. C.; Li, Q.; Lu, Y. Y.; Luo, H. Y.; Jian, Y. H.; Li, D. W.; Kong, D. P.; Wang, R. H.; Tan, J. B.; Cai, Z. M. et al. Laser direct writing of flexible thermal flow sensors. *Nano Lett.* **2023**, *23*, 10317–10325.

[31] Chen, H. X.; Qian, M. D.; Yu, K.; Liu, Y. F. Low threshold microlasers based on organic-conjugated polymers. *Front. Chem.* **2021**, *9*, 807605.

[32] Wang, W.; Chen, Z. Q.; Lin, B.; Liu, M. C.; Zhang, Y.; Liu, S. J.; Li, Y.; Zhao, Q. Two-photon polymerization-based 3D micro-scaffolds toward biomedical devices. *Chem. Eng. J.* **2024**, *493*, 152469.

[33] Wang, H.; Zhang, Y. L.; Wang, W.; Ding, H.; Sun, H. B. On-chip

laser processing for the development of multifunctional microfluidic chips. *Laser Photonics Rev.* **2017**, *11*, 1600116.
[34] Wang, W.; Han, B.; Zhang, Y.; Li, Q.; Zhang, Y. L.; Han, D. D.; Sun, H. B. Laser-induced graphene tapes as origami and stick-on labels for photothermal manipulation via marangoni effect. *Adv. Funct. Mater.* **2021**, *31*, 2006179.
[35] Wang, W.; Liu, Y. Q.; Liu, Y.; Han, B.; Wang, H.; Han, D. D.; Wang, J. N.; Zhang, Y. L.; Sun, H. B. Direct laser writing of superhydrophobic PDMS elastomers for controllable manipulation via marangoni effect. *Adv. Funct. Mater.* **2017**, *27*, 1702946.
[36] Li, C.; Zhao, J. H.; Yang, Y.; Chen, Q. D.; Chen, Z. G.; Sun, H. B. Sub-bandgap photo-response of chromium hyperdoped black silicon photodetector fabricated by femtosecond laser pulses. *IEEE Sensors J.* **2021**, *21*, 25695–25702.
[37] Yong, J. L.; Li, X. L.; Hu, Y. D.; Wang, Y. M.; Peng, Y. B.; Chen, Z. R.; Zhang, Y. C.; Zhu, S. W.; Wang, C. W.; Wu, D. Portable triboelectric electrostatic tweezer for external manipulation of droplets within a closed femtosecond laser-treated superhydrophobic system. *Nano Lett.* **2024**, *24*, 7116–7124.
[38] Xia, S.; Wang, M.; Gao, G. H. Preparation and application of graphene-based wearable sensors. *Nano Res.* **2022**, *15*, 9850–9865.
[39] Lu, Y. Y.; Yang, G.; Wang, S. Q.; Zhang, Y. Q.; Jian, Y. H.; He, L.; Yu, T.; Luo, H. Y.; Kong, D. P.; Xianyu, Y. L. et al. Stretchable graphene-hydrogel interfaces for wearable and implantable bioelectronics. *Nat. Electron.* **2023**, *7*, 51–65.
[40] Ma, Z. Q.; Khoo, B. L. Recent advances in laser-induced-graphene-based soft skin electronics for intelligent healthcare. *Soft Sci.* **2024**, *4*, 26.
[41] Wang, H. M.; Li, S.; Wang, Y. L.; Wang, H. M.; Shen, X. Y.; Zhang, M. C.; Lu, H. J.; He, M. S.; Zhang, Y. Y. Bioinspired fluffy fabric with *in situ* grown carbon nanotubes for ultrasensitive wearable airflow sensor. *Adv. Mater.* **2020**, *32*, 1908214.
[42] Li, M. W.; Zhang, T.; Wang, P. C.; Li, M. H.; Wang, J. Q.; Liu, Z. W. Temperature characteristics of a pressure sensor based on BN/graphene/BN heterostructure. *Sensors* **2019**, *19*, 2223.
[43] Han, S. Q.; Zhou, S. Y.; Mei, L. Y.; Guo, M. L.; Zhang, H. Y.; Li, Q. N.; Zhang, S.; Niu, Y. K.; Zhuang, Y.; Geng, W. P. et al. Nanoelectromechanical temperature sensor based on piezoresistive properties of suspended graphene film. *Nanomaterials* **2023**, *13*, 1103.
[44] Liu, D. Q.; Chen, S. Y.; Lu, Z. T.; Ma, N.; Sun, Y. Q. Temperature sensor based on temperature and frequency dependence of graphene impedance. *J. Phys. D: Appl. Phys.* **2019**, *52*, 075102.

This is an open access article under the terms of the Creative Commons Attribution 4.0 International License (CC BY 4.0, https://creativecommons.org/licenses/by/4.0/).

© The Author(s) 2025. Published by Tsinghua University Press.